Monodisperse Gold Nanotriangles: Size Control, Large-Scale Self-Assembly, and Performance in Surface-Enhanced Raman Scattering

Leonardo Scarabelli,[†,§] Marc Coronado-Puchau,[†,§] Juan J. Giner-Casares,[†] Judith Langer,[†] and Luis M. Liz-Marzán[†,‡,*]

[†]Bionanoplasmonics Laboratory, CIC biomaGUNE, Paseo de Miramón 182, 20009 Donostia, San Sebastián, Spain and [‡]Ikerbasque, Basque Foundation for Science, 48011 Bilbao, Spain. [§]L. Scarabelli and M. Coronado-Puchau contributed equally.

ABSTRACT Au nanotriangles display interesting nanoplasmonic features with potential application in various fields. However, such applications have been hindered by the lack of efficient synthetic methods yielding sufficient size and shape monodispersity, as well as by insufficient morphological stability. We present here a synthesis and purification protocol that efficiently addresses these issues. The size of the nanotriangles can be tuned within a wide range by simply changing the experimental parameters. The obtained monodispersity leads to extended self-assembly, not only on electron microscopy grids but also at the air—liquid interface, allowing transfer onto centimeter-size substrates. These extended monolayers show promising performance as surface-enhanced Raman scattering substrates, as demonstrated for thiophenol detection.

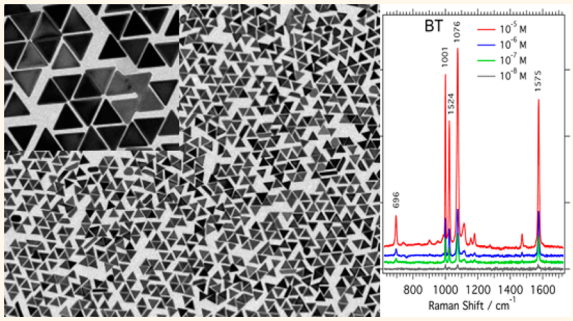

KEYWORDS: gold · nanotriangles · shape separation · interfacial self-assembly · SERS

The requirement of new methods for the synthesis of plasmonic nanoparticles (NPs) with well-defined shape and monodispersity has grown hand in hand with the increasing number of challenges involved in nanoscience and nanotechnology. Ultrasensitive detection,[1] metamaterials,[2] and drug delivery[3,4] are prominent examples among a broad array of promising applications requiring a fine control on the synthetic process of the NPs. Localized surface plasmon resonances (LSPRs) are the main features of plasmonic NPs. Therefore, tuning the LSPR band position in the UV—vis—NIR region is the most important prerequisite for the successful application of a synthesis method.[5] The position and the width of LSPR bands are directly linked to NP shape,[6−8] size,[9] and organization.[10,11]

One of the most influencing breakthroughs in this field is the seed-mediated growth of gold NPs. Proposed in the early 2000s by various groups,[12−15] this method is based on the temporal separation of nucleation and growth for a better control of the synthesis. The premade seeds (typically <5 nm spherical particles) act as both catalysts and nucleation points for the growth of gold NPs. Metal reduction onto the seed particles is controlled in such a way that a symmetry-breaking event occurs, thus providing an advantageous method for the growth of particles with anisotropic shapes such as nanorods and nanostars. Au nanorods are one of the most studied NPs in this context,[16,17] due to the availability of synthetic methods that allow one to routinely achieve shape-yields up to 99%.[18] Mirkin's group recently reported a thorough study of NP growth on cetyltrimethylammonium chloride (CTAC)-capped seeds. In short, the use of different halogen counter-anions, both in the presence and in the absence of silver cations,[19] is crucial in the synthesis of noble metal NPs of different shapes.[20] In this context, Au nanotriangles (NTs) stand out for their unique optical and plasmonic properties. However, the quality of available Au NTs is still far away from that usually found for Au nanorods. The yield of common synthetic

* Address correspondence to llizmarzan@cicbiomagune.es.

Received for review February 6, 2014 and accepted May 21, 2014.

Published online May 21, 2014
10.1021/nn500727w

methods for Au NTs is usually below 30−40%, and the particles often show high polydispersity. Indeed, in the existing synthetic protocols the NTs usually have relatively big lateral dimensions,[7,21] and no synthetic protocols for the preparation of monodisperse Au NTs below 100 nm are available in the literature. Moreover, the stability of these NPs against oxidation is low, and reshaping typically takes place a few hours after their preparation.[22] All these factors have seriously hindered the application of Au NTs for the development of plasmonic devices.

Since it is not always possible to synthesize highly monodisperse AuNPs in one step, different purification strategies have been developed to obtain high-quality NP colloids. Originally Jana *et al*. proposed a separation technique for pentatwinned Au nanorods, based on sedimentation triggered by increasing the surfactant concentration.[23] More recently Park *et al*. extended this depletion-induced separation to other NP shapes by quantitatively studying the depletion energy as a function of the area of interaction.[24] We demonstrate here that variations of these synthetic processes can yield Au NTs with initial shape-yield higher than 50%, which can be further increased up to 95% after a simple and fast purification step. This method additionally yields optimum monodispersity of the Au NTs down to 4% and a wide tunability of the NT dimensions with edge lengths ranging from 50 to 150 nm, which translates into LSPR values from 630 to 740 nm. This high uniformity allowed us to assemble monodisperse Au NTs on substrates and to evaluate their performance for sensing applications. In this respect, we aim at the formation of close-packed Au NT monolayers for their use as surface-enhanced Raman scattering (SERS) substrates. SERS is an advanced analysis technique that can be used for the ultradetection of a vast array of analytes of interest in different fields, *e.g*., biology, medicine, and environment.[25] Still, SERS ultradetection usually requires the formation of hot spots, *i.e*., short separation distances between the plasmonic nanoparticles.[26] This requirement can be satisfied by the self-assembly of nanoparticles, which can be improved at the air−liquid interface, into large monolayers of closely packed nanoparticles.[27,28] Since the Au NTs are stable in aqueous solution, surface activity can be obtained through functionalization with polyvinylpyrrolidone (PVP).[29,30] PVP coating of plasmonic nanoparticles allows the formation of single-nanoparticle monolayers at the air−liquid interface extended over large areas reaching square centimeters, as has been previously shown for silver nanocubes[31] and nanotriangles.[32] We therefore used PVP coating and subsequent self-assembly for fabricating SERS substrates based on Au NTs. The SERS performance of both Au NTs in solution and assemblies is demonstrated through benzenethiol detection, reaching enhancement factors around 10^5, even for single Au NTs in solution.

RESULTS AND DISCUSSION

The experimental approach for the synthesis of Au NTs involves three consecutive steps: (1) generation of CTAC-coated Au seeds, (2) fast addition of the generated seeds to a final growth solution, and (3) purification of the products (see Scheme S1, Supporting Information (SI)).

Synthesis of Au NTs. The synthesis of Au NTs is based on the seed-mediated growth originally proposed by Mirkin and co-workers.[19] In this method, the presence of iodide anions in a silver-free growth solution triggers the anisotropic growth of the CTAC-coated seeds. The initial Au seeds with a size of *ca*. 7 nm are first overgrown up to 40 nm in an intermediate growth step and subsequently transferred to the final growth solution, yielding an overall shape-yield around 30%, with rather high polydispersity. Interestingly, we demonstrate that the shape-yield and monodispersity of the NTs were significantly improved by overgrowing the seeds in the presence of iodide prior to transfer into the final growth solution, before the reaction was completed. It is important to mention at this point that in previous reports size tunability by overgrowth reactions was limited by the initial particle size, which was typically more than 150 nm.[21] In the present work, small Au NTs with edge lengths down to 60 nm were obtained for the first time, thereby leading to a significant improvement in size tunability.

This synthetic scheme comprising two growth steps is similar to that proposed by Jana and Murphy in 2001 for the early synthesis of gold nanorods,[33] in which the particles were transferred while the "intermediate" growth was still ongoing. Furthermore, the yield in NTs was significantly increased (above 50%) by the "fast seed addition" and other modifications described in more detail in the Experimental Section (Figure 1A and Figure S1, SI). The Au NTs obtained in this way are considerably smaller (edge length 71 ± 3 nm, Figure 1B) and characterized by a low polydispersity (below 6%, see Figure S2, SI). High-resolution TEM (HR-TEM) confirmed the {111} nature of the planar facets of the Au NTs (Figure 1D). HR-SEM analysis revealed the presence of a twin plane parallel to the most extended facets, leading to the formation of NTs with a truncated-bipyramid morphology (see Figure 1C), where also the lateral facets are of the {111} family. Strikingly, the introduction of the fast addition during seed overgrowth does not seem to affect the reproducibility of the synthetic protocol, even when the synthesis was scaled up to 250 mL (Figure S3, SI). Regarding the stability of the Au NTs over time, UV−vis monitoring was carried out to detect optical changes in the NT solution. In contrast with previous reports, the Au NTs presented here were stable for at least 3 months, and no reshaping was observed (Figure S4, SI).

Although a complete comprehension of the growth mechanism is beyond the aim of this work, our observations lead to some interesting reflections. The first observation is that, following the original procedure proposed by Mirkin *et al.*, the seed overgrowth step is indispensable for the formation of Au NTs. In fact, in a control experiment skipping this step, both UV–vis and TEM analysis confirmed that almost no Au NTs were obtained (Figure S5, SI). Yet, what makes this step crucial is not clear: Is the growth pathway just influenced by the increased size of the seed? Does the different crystallographic structure of the bigger particles play a relevant role? Or do both phenomena contribute equally? We found that the fast addition introduced here prevents the seed from growing completely prior to transfer into the growth solution, which suggests that the size of the particles used as seeds is not a crucial parameter or at least that it is not the only one. Additionally, we achieved a significant increase in shape-yield by introducing a small amount of iodide in the overgrowth medium (see Experimental Section). Therefore, our experimental data suggest that this intermediate step may be relevant for the modification of the crystallographic structure of the seeds, which is crucial for the required symmetry-breaking event.[34,35] This effect can be somehow verified by analyzing the overgrown seeds by both UV–vis spectroscopy and TEM analysis. A clear red shift of the plasmon band can be observed when iodide ions are present in the overgrowth medium (Figure 2A), and we found a significant amount of seeds with triangular shape (Figure 2B,C). To further confirm our observations, we directly synthesized the initial seeds in the presence of iodide. Interestingly, using these seeds, the overgrowth step is not necessary to achieve a final triangular shape, even if the quality of the sample in terms of monodispersity is strongly affected (Figure S6). It is important to underline that although our results are not exhaustive, it is obvious that iodide has a strong effect on the shape of the seeds and on their further growth, which is essential to drive the symmetry-breaking event toward the development of a triangular shape.

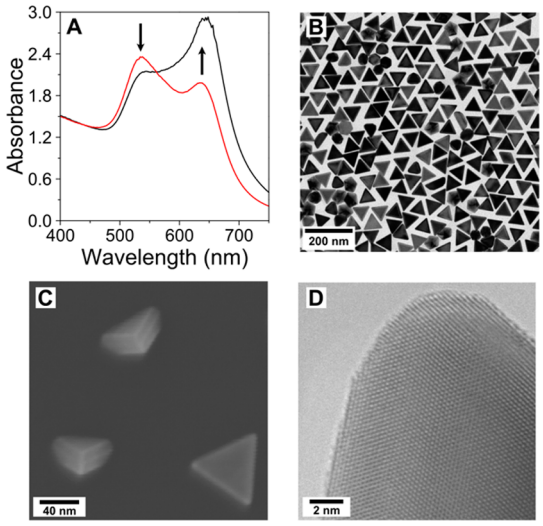

Figure 1. Synthesis of Au NTs. (A) UV–vis spectra of samples obtained with (black line) and without fast addition (red line). Notice the different intensity ratio between the byproduct band (isotropic nanoparticles, maximum around 520–530 nm) and the band corresponding to the NTs (around 650 nm). (B) TEM images of Au NTs prepared with fast addition. Additional TEM images are provided in the SI, Figure S2. (C) HR-SEM image of Au NTs where a twin plane in the middle of the particle can be clearly distinguished. (D) HR-TEM image of the area near a tip of a Au NT.

Nanotriangle Purification. Although the yield and monodispersity of the Au NTs were improved by this synthesis method, still a considerable amount of byproduct particles are present, which may hinder the direct use of these NTs for applications that require very high particle monodispersity and narrow plasmon resonances. In order to obtain a pure Au NT dispersion, purification by flocculation and subsequent precipitation was explored. Such a separation by shape can be achieved by exploiting the depletion interactions between particles, in the presence of micelles. This kind of interaction arises when two particles are separated by a distance that is smaller than the size of a more

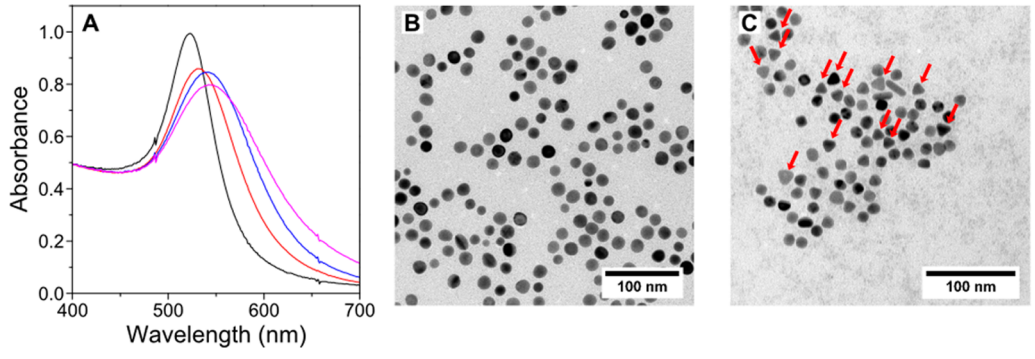

Figure 2. Iodide effect on the seed overgrowth step. (A) UV–vis spectra of the fully overgrown seeds in the presence of different amounts of a 0.01 M NaI solution: 0 μL (black line), 15 μL (red line), 30 μL (blue line), and 60 μL (pink line). (B) TEM image of seeds overgrown in the absence of iodide. (C) TEM image of seeds overgrown in the presence of 60 μL of a 0.01 M NaI solution (pink line in A); seeds that clearly show a triangular shape are labeled with red arrows.

abundant second component,[36−38] which, in our case, is represented by hexadecyltrimethylammonium chloride (CTAC) micelles. This approach presents two crucial benefits: (1) the stability of the Au NTs is not compromised at high CTAC concentrations (indeed, CTAC can even enhance the stability of Au NTs) and (2) centrifugation is not necessary due to the nature of the CTAC stock solution (see Experimental Section). These two highlighted aspects allowed us to purify the Au NTs in a simple and non-time-consuming way. Different CTAC concentrations were explored to find the optimal purification conditions, in which a high purity of the precipitate is achieved along with a good purification yield, *i.e.*, a large proportion of the initial NTs are precipitated. The results are summarized in Figure 3. The separation of the byproduct (mainly isotropic particles) can be clearly appreciated by a significant color change of the solution from dark blue to indigo. Moreover the purification is highlighted by the change in intensity ratio between the two LSPR bands: indeed, the band centered at 520−530 nm (typical of isotropic particles) significantly decreased. The optimal procedure was found to correspond to a CTAC concentration of 0.15 M. As shown in Figure 3, 0.125 M CTAC leads to highly pure Au NTs, but in an extremely low amount, while when using higher CTAC concentrations (from 0.175 to 0.4 M), the separation was not completed. In addition, a second purification step can be carried out, but the increment in purification yield is negligible compared to the amount of NTs found in the supernatant (Figure S7, SI). TEM analysis confirmed the separation of NTs: while the supernatant mainly comprised different quasi-isotropic particles (Figure 3B), the purity level of NTs in the precipitate was higher than 90% (Figures 3D and S8−10, SI). Interestingly, this purification procedure is extremely robust and efficient regardless of the original NT shape-yield achieved in the synthesis. Therefore, the overall process is robust and highly reproducible (Figure S11).

The equation proposed by Park *et al*. to calculate the depletion interaction energy was adapted for these NTs:

$$|U| = \frac{2r_m l^2 \sqrt{3} N_0 (c - \mathrm{cmc})}{4Q} k_B T \qquad (1)$$

where k_B is Boltzman's constant, N_0 is Avogadro's number, c is the molar concentration of the surfactant, cmc is the critical micelle concentration, Q is the aggregation number, r_m is the micellar radius, and A is the area of interaction of the two particles, which in our case is equal to $(l^2\sqrt{3})/4$, with l the edge of one NT. The 0.15 M concentration that we selected as the best choice corresponds to a value of $|U|$ equal to $9.8k_BT$ (literature values of 0.001 M, 120, and 3 nm were used for CTAC cmc, aggregation number, and micelle radius, respectively[39,40]). This value is almost double the predicted value of $4-5k_BT$ proposed by Park *et al*.[24]

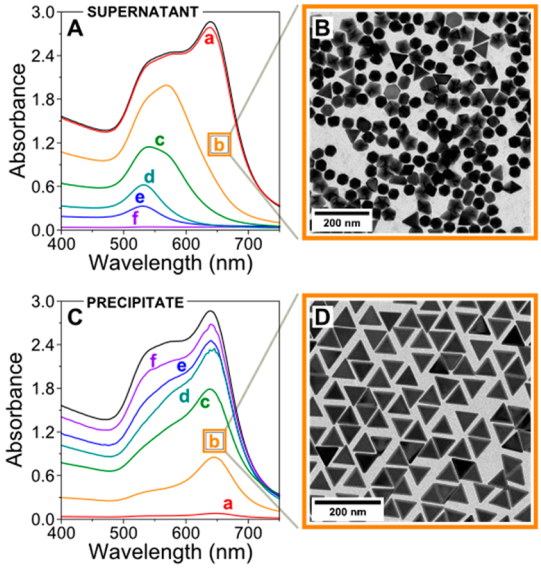

Figure 3. Influence of CTAC concentration on the purification of Au NTs. (A) UV−vis spectra of the supernatant solutions: (a) 0.125 M, (b) 0.15 M, (c) 0.175 M, (d) 0.2 M, (e) 0.3 M, (f) 0.4 M. As expected, an increase in surfactant concentration leads to a more extensive flocculation/precipitation; the black line represents the original sample. (B) TEM image of the 0.14 M (b) supernatant. (C) UV−vis spectra of the precipitate after redispersion in 0.1 M CTAC solution, as indicated in A. Note the different intensity ratios between the two LSPR bands. (D) TEM image of the 0.14 M (b) precipitate. Additional TEM images are provided in the SI, Figures S8, S9.

This difference can be explained considering that the sides of the NTs are not perpendicular to the most extended crystallographic facets; that is, using the TEM images as a reference, the area of interaction is significantly overestimated.

Size Tunability. This improved synthesis method allowed us to explore the size tunability of the Au NTs. This objective was partially achieved by simply varying the amount of seed transferred into the growth solution by fast addition. In fact, by decreasing the amount of seeds, the NTs' edge length could be increased up to 90 nm (Figure 4). However, further reduction in seed concentration leads to a polydispersity increase, from less than 6% up to 15% (Figure S12, SI). This can be understood considering that the iodide/seed ratio is also varied; it is known that iodide can strongly bind to the gold surface, so that the growth of the particles can be significantly affected.[7,19,41] Therefore, by lowering the concentration of iodide down to 50 μM (see Experimental Section), the edge length of the NTs further increased up to 150 nm (Figure 4). As expected, this increase in edge length leads to a red shift of the plasmon band (Figure S13, SI).

The purification procedure (described above) could also be used for all the different Au NT sizes (see Figures S14−S18, SI). In all cases, purity higher than 90% and high monodispersity around 6% were achieved. The CTAC concentrations used for each size,

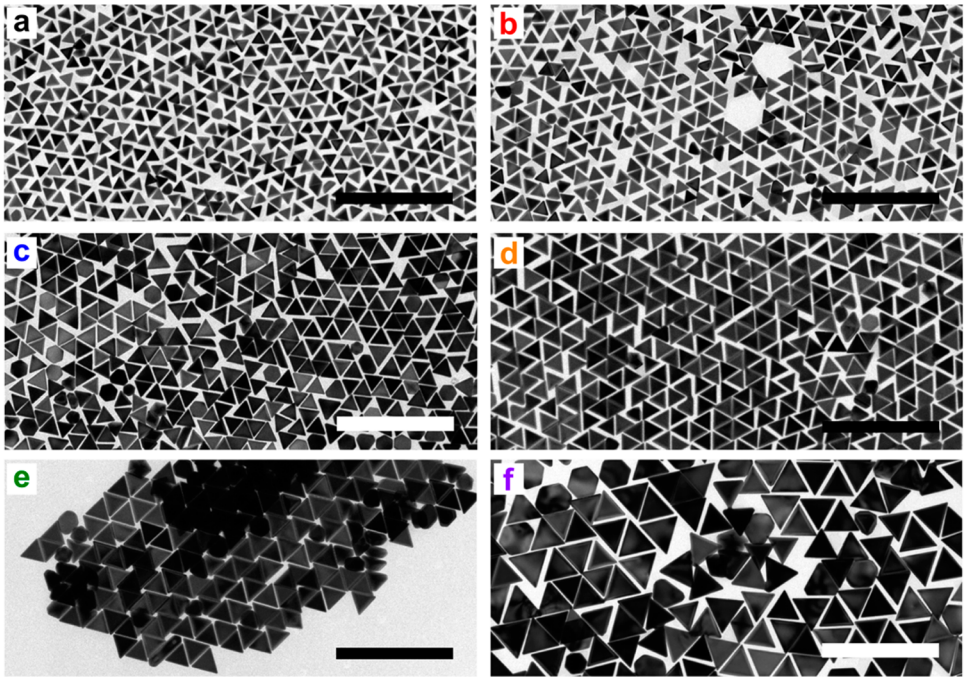

Figure 4. Size tunability of Au NTs: TEM analysis. TEM images of Au NTs with increasing edge lengths. Sample b was prepared through the standard synthesis procedure depicted in Figure 1. c–f were prepared by using different amounts of seed solution transferred into the growth solution: 1.2 mL (a), 800 μL (b), 600 μL (c), 400 μL (d), 200 μL (e), and 100 μL (f). Scale bars: 500 nm.

TABLE 1. TEM Analysis of Au NTs Size for the Samples Shown in Figure 4 and Figure 5,[a]

seed (μL)	edge (nm)	polidispersity (%)	area (nm^2)	[CTAC] (M)	$\|U\|$ (k_BT)
100	147 ± 10	6.68	9348	0.035	9.6
200	110 ± 5	4.66	5257	0.065	10.1
400	87 ± 5	5.89	3292	0.1	9.8
600	78 ± 6	6.05	2604	0.125	9.7
800	68 ± 3	4.02	1983	0.15	8.9
1200	59 ± 2	3.84	1513	0.2	9.1

[a] The edge length was calculated as an average over 200 NTs. The value of $|U|$ was calculated according to eq 1.

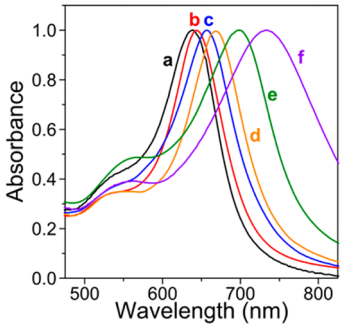

Figure 5. UV–vis spectra of the Au NTs depicted in Figure 4 (normalized at the LSPR maximum). The spectra are labeled as shown in Figure 4.

together with the calculated energy potential for the depletion interaction ($|U|$), are depicted in Table 1. Interestingly, in all cases the energy values are around $9k_BT$, which means that this purification procedure could be applied to other flat nanoparticles of previously known dimensions. For this range of NT size the LSPR band varied between 630 and 750 nm (Figure 5). A linear correlation was found between the NT dimension and the maximum of the LSPR band (Figure S19, SI). The low LSPR wavelengths (typical literature values are above 1000 nm), together with the strong scattering that can be seen from the colloidal solution, suggest that the Au NTs prepared with our method are rather thick, in agreement with SEM images (Figure 1C). Similarly to what happens in the case of short Au nanorods, the quadrupolar mode is not observed in the UV–vis analysis, as a consequence of the low aspect ratio of the NTs.[42] This observation was also confirmed by TEM analysis of vertically positioned NTs, which revealed an average thickness of 30 nm (see Figure S20, SI).

Self-Assembly of Au NTs. Au NTs@PVP (see Experimental Section) were transferred (by centrifugation and redispersion) into an ethanol–hexane mixture with a volume ratio of 2:3 and subsequently spread on top of an air–liquid interface. PVP provides surface activity to the Au NTs, resulting in the stabilization of a monolayer of the Au NTs at the air–liquid interface covering an area of several square centimeters. The amount of Au NTs to be spread was estimated from the NT concentration in solution to obtain a single monolayer at the air–liquid interface. The monolayer appears as a thin gold layer to the naked eye (Figure 6A) and can be readily transferred onto any solid substrate by gently touching the monolayer with a substrate parallel to the air–liquid interface. This assembly method requires a

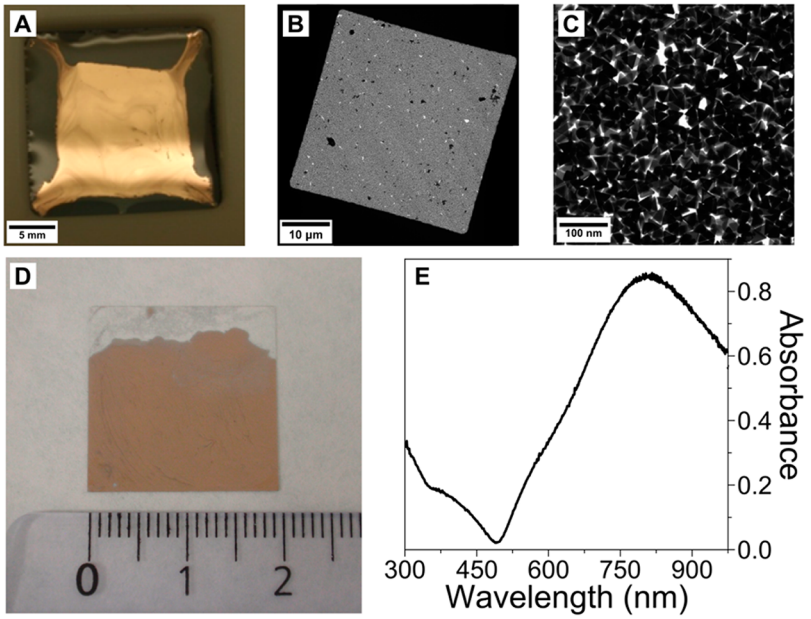

Figure 6. Self-assembly of Au NTs@PVP. (A) Optical photograph of a AuNT@PVP monolayer organized at the air−water interface. (B, C) TEM images of a Au NT@PVP monolayer upon transfer onto a TEM grid (additional TEM images are provided in the SI, Figure S21). (D) Optical photograph of a AuNT@PVP monolayer on a glass slide. The scale is indicated by the ruler. (E) UV−vis spectrum of the Au NTs monolayer transferred onto a transparent glass substrate. The absorption maximum of the LSPR band is located at *ca.* 810 nm.

small amount of sample, given that the whole amount of Au NTs spread at the air−liquid interface will enter the monolayer. Moreover, this method can be scaled up to any required area, as shown in Figure 6D (SI) for a 2×2 cm^2 glass. The possibility of fabricating homogeneous substrates over large areas is most relevant, especially when comparing with methods such as drop casting. Drop casting allows the fabrication of crystallites limited to the micrometer range,[43] while achieving only local order due to coffee ring effects.[44]

The Au NT monolayer was transferred onto a carbon-coated grid for TEM analysis. The NTs within the monolayer showed a high degree of local disorder; however, they were positioned within short distances from each other (Figure 6B,C). ImageJ software was used to calculate the coverage density, which resulted to be $89 \pm 9\%$, as an average value over 60 TEM images (Figure 6D). This short interparticle distance is most relevant for a successful performance in SERS spectroscopy experiments, as shown below. Indeed, strong plasmon coupling was observed by UV−vis spectroscopy on such a Au NTs monolayer (Figure 6E) revealed by a significant LSPR shift of more than 150 nm, from *ca.* 650 nm in bulk solution up to *ca.* 810 nm in the film.

SERS Performance. The plasmonic response of the Au NTs allowed us to study their SERS performance, both in solution from well-separated nanoparticles (no aggregation) and from solid substrates, where plasmon coupling due to close proximity is expected. SERS was measured in aqueous solution using molecules with different binding affinities toward Au nanoparticles, namely, the thiols benzenethiol (BT) and 4-mercaptopyridine (4-MP), the dye crystal violet (CV), and the explosive 2,4-dinitrotoluene (2,4-DNT). BT binds covalently to the Au surface *via* formation of the 2.3 eV strong Au−S bond,[45,46] whereas the polar 4-MP preferentially binds *via* the thiol group but can also interact *via* the pyridine nitrogen. In the cationic CV, the electrostatic bond is stronger than in the neutral 2,4-DNT, which interacts *via* nitro groups with the Au NPs. Figure 7A shows the SERS spectra of BT at different concentrations ranging from 10^{-5} to 10^{-8} M. The characteristic vibrations observed at 1575, 1076, 1025, 1001, and 696 cm^{-1} can be clearly identified for BT concentrations down to 10^{-7} M, whereas the spectrum at 10^{-8} M shows the three most intense vibrations, with less intense vibrations being below the detection limit. All the detected vibrational modes are in good agreement with reported SERS spectra for BT,[47] with the peaks between 1600 and 900 cm^{-1} assigned to ring deformation modes, namely, C−C asymmetric stretching, ring in-plane deformation, C−C symmetric stretching, ring out-of-plane deformation, and C−H out-of-plane bending. The low-frequency modes at 473 and 417 cm^{-1} correspond to the C−S out-of-plane bending and C−S stretching combined with the ring in-plane deformation mode, respectively.[48,49] The polar 4-MP shows a very strong signal only at high concentration (10^{-5} M) but it rapidly decreased by a factor 70 for 10^{-6} M (Figure S22, SI). Most intense modes were found at 1576, 1096, 1065, 1003, and 998 cm^{-1}, in agreement with earlier reports.[50−52] The SERS spectrum from a 10^{-8} M 4-MP solution exhibits a very low signal-to-noise ratio, and only the most intense mode at 1065 cm^{-1} could be

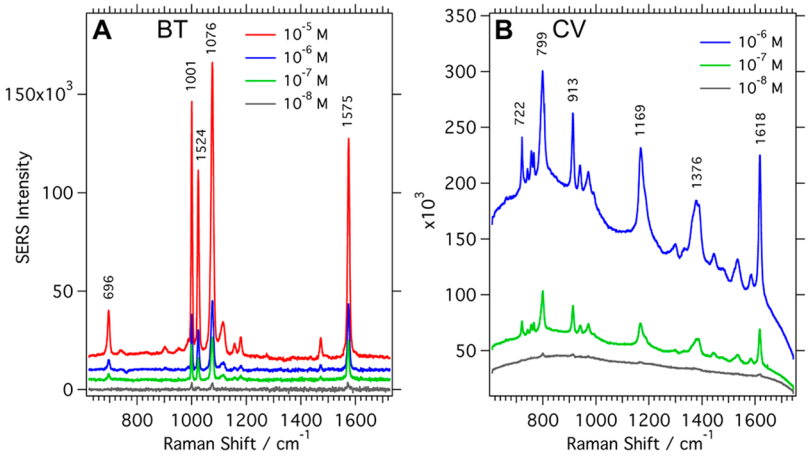

Figure 7. SERS performance of Au NTs in solution. SERS spectra of BT excited at 785 nm (A) and CV excited at 633 nm (B), with concentrations varying between 10^{-5} and 10^{-8} M. In A an offset was applied to improve data presentation. In B the SERS spectra are not background corrected, showing significant fluorescence from dissolved CV, and are presented without offset.

detected, with 600-fold lower intensity compared to the 10^{-5} M solution. Figure 7B shows the surface-enhanced resonant Raman scattering spectra for CV with concentrations ranging between 10^{-6} and 10^{-8} M, at an excitation wavelength of 633 nm. Whereas very strong SERS signals were detected from 10^{-6} to 10^{-7} M, the intensities at 10^{-8} M are low with respect to the background, but all the main modes at 1618, 1376, 1169, 913, 799, and 722 cm^{-1} can be clearly identified. The background is related to CV fluorescence, probably originated from free molecules in solution. At an excitation wavelength of 785 nm, the fluorescence background significantly decreases, but also SERS is found to be less efficient (Figure S22, SI), as expected when the resonance condition is lost. A lower SERS response was observed for the explosive 2,4-DNT. The two dominant modes at 1345 and 881 cm^{-1} corresponding to NO_2 stretch and bending out-of plane modes could be detected only down to 10^{-4} M (Figure S22, SI),[53] most likely because of the lower affinity of the analyte to the Au surface.

Quantification of the SERS performance was carried out through determination of the enhancement factor. In colloidal dispersions, the analytical enhancement factor (AEF) of a nanoparticle ensemble can be estimated through the ratio between the SERS intensity for the selected mode of a given analyte (I_{SERS}) and the corresponding Raman intensity (I_{RS}) under identical experimental conditions (sample preparation, laser wavelength and power, objectives, exposition time, *etc.*), using the following equation:[54]

$$\mathrm{AEF} = \frac{I_{SERS}}{I_{RS}} \frac{c_{RS}}{c_{SERS}} \qquad (2)$$

where C_{SERS} and C_{RS} are the concentrations of the analyte in the SERS and Raman experiments, respectively. Additional contribution to SERS originating from molecular resonances upon 785 nm excitation were avoided by using the nonresonant BT as analyte for AEF estimation. With $c_{RS} = 10^{-1}$ M, $c_{SERS} = 10^{-7}$ M, I_{RS} (1002 cm^{-1}) = 6094, and I_{SERS} (999 cm^{-1}) = 708, the AEF was estimated to be 1.2×10^5. This value lies within the highest AEF presented in the literature for metal nanoparticle colloids.[54]

The SERS performance of dense Au NT monolayers was studied using the same analytes with concentrations ranging from 10^{-5} to 10^{-8} M. Figure 8 shows the average SERS spectra of BT measured on an Au NT assembly on a glass slide and of CV on Au NTs assembled on a TEM grid. The detection limit for BT was found to be 10^{-7} M, which is 1 order of magnitude higher than in solution. At lower BT concentrations the SERS signature could not be unambiguously resolved because of interference with background bands originating from PVP and other contaminations. In contrast, CV could be detected on the assembled films down to the same level as in solution, without interference with signals originating from the background at an excitation wavelength of 633 nm (Figure 8B). SERS mapping of the Au NTs assembly containing BT was carried out to study the intensity distribution over larger areas. The SERS images for the vibrations at 1075 and 1575 cm^{-1} over a surface area of *ca.* 80 μm^2 show nearly identical signal distribution of areas with higher and lower intensities (brighter and darker spots) for both modes (see insets in Figure 8A). The fluctuations can be related to the formation of hotspots with different electromagnetic field enhancement, due to the random order of Au NTs. Walker *et al.* showed that the SERS efficiency of randomly assembled Au NTs is *ca.* 1 order of magnitude lower than that for the corresponding ordered crystalline assembly over a small area within a coffee ring.[43] The observed variation of the intensity ratio can be caused by small changes of the molecular orientation with respect to the surface, leading to different mode-dependent SERS cross sections. Nonetheless, the SERS intensity in our samples is relatively homogeneous, and thus this system is a promising candidate

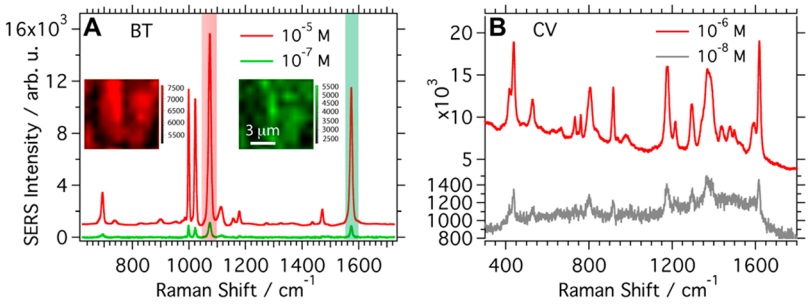

Figure 8. SERS performance of self-assembled Au NTs. Concentration-dependent average SERS spectra obtained from a large-scale mapping of BT excited with 785 nm (A) and CV excited with 633 nm (B) onto a Au NT monolayer. The insets in A are SERS maps of the scanned area ($9 \times 9\ \mu m^2$) for two characteristic vibrations at 1075 cm^{-1} (red) and 1575 cm^{-1} (green) for a BT concentration of 10^{-7} M (green spectrum). The SERS spectra in B are not background corrected and are presented without offset.

for SERS applications along with other anisotropic Au NPs such as nanostars and nanorods.

CONCLUSIONS

We have demonstrated an improved synthesis of Au nanotriangles with sizes ranging from 50 to 150 nm edge length. In all cases the Au NTs exhibited a high monodispersity, down to 3% SD, and a high shape-yield above 50%. A fast and simple purification step allowed separation of the byproducts, thereby reaching a 95% NT shape-yield. The high quality of these solutions, together with the unique optical properties of the Au NTs, renders them promising candidates for the development of nanoplasmonic devices. We illustrated this possibility by assembling NTs at the air–liquid interface, obtaining monolayers with dimensions that could be easily increased up to several square centimeters. The SERS performance was tested by detection of BT, 4-MP, CV, and 2,4-DNT within the concentration range of 10^{-5} to 10^{-8} M, and a remarkable AEF of 1.2×10^5 was obtained for a BT solution.

EXPERIMENTAL SECTION

Materials. Hexadecyltrimethylammonium chloride (CTAC, 25 wt % in water), hydrogen tetrachloroaurate trihydrate ($HAuCl_4 \cdot H_2O$, ≥99.9%), L-ascorbic acid (≥99%), polyvinylpyrrolidone (PVP, average molecular weight: 10 000), thiophenol (>98%), sodium iodide (≥99.5%), sodium borohydride ($NaBH_4$, 99%), hexane (≥95%), and ethanol (>99.9%, absolute grade) were purchased from Aldrich. All chemicals were used as received. Milli-Q water (resistivity 18.2 MΩ · cm at 25 °C) was used in all experiments. All glassware was washed with aqua regia, rinsed with water, sonicated three times for 3 min with Milli-Q water, and dried before use.

Synthesis of Au Seed@CTAC. The initial seeds were prepared by the standard CTAC/$NaBH_4$ procedure: 25 μL of a 0.05 M $HAuCl_4$ solution was added to 4.7 mL of 0.1 M CTAC solution; 300 μL of a freshly prepared 0.01 M $NaBH_4$ solution was then injected under vigorous stirring. Excess borohydride was consumed by keeping the seed solution for 2 h at room temperature prior to use.

Synthesis of Au NTs@CTAC. In a typical synthesis of 40 mL of a Au NT solution the following two growth solutions were prepared: (1) 1.6 mL of a 0.1 M CTAC solution was added to 8 mL of Milli-Q water, followed by 40 μL of 0.05 M $HAuCl_4$ solution and 15 μL of a 0.01 M NaI solution; (2) 500 μL of a 0.05 M $HAuCl_4$ solution was added to 40 mL of 0.05 M CTAC, followed by 300 μL of a 0.01 M NaI solution. The first solution was used to grow the CTAC-capped seed into larger nanoparticles, while the second solution was used as the NT growth batch. Before proceeding, the initial seed@CTAC solution was diluted 10× in a 0.1 M CTAC solution. Subsequently, 40 and 400 μL of 0.1 M AA solution were added to solutions 1 and 2, respectively, and both solutions were manually stirred until the complete transparency of the solutions was achieved, indicating Au^{III} to Au^{I} reduction. Finally, 100 μL of diluted seed@CTAC solution was added to solution 1 (and manually stirred for 1 s), and immediately 3.2 mL of this solution was added to solution 2 (and manually stirred for a few seconds). The Au NT dispersion was left undisturbed at room temperature for at least 1 h (see SI, Scheme S1, for a schematic representation of the synthetic protocol). We observed that addition of 15 μL of a 0.01 M NaI solution to solution 1 further improved the yield in NTs obtained with the fast addition procedure.

Purification of the Au NTs. After spectroscopic characterization, the Au NT dispersion was purified by addition of a selected amount of 25 wt % CTAC solution (the final concentration for optimal purification is depicted in the main text and related SI). Flocculation of the Au NTs was completed overnight, the supernatant was then removed, and the precipitated particles were redispersed in 5 mL of 0.1 M CTAC solution. Typically the concentration in Au^0 of the purified sample was around 1.75 mM (estimated using the absorbance at 400 nm[55,56]).

PVP Coating of Au NTs. Au NTs@CTAC were centrifuged (4000 rpm, 15 min, 30 °C), and the supernatant was carefully removed. The pellet was redispersed in 50 μL of a 0.1 M CTAC solution and sonicated briefly. Subsequently, water was added to reach a Au^0 concentration of 0.5 mM. A 10 mg/mL PVP solution was prepared, sonicated for 10 min, and finally added under vigorous stirring to the Au NTs to achieve a final PVP concentration of 1 mg/mL. This solution was stirred overnight at room temperature.

Self-Assembly of the Au NTs@PVP at the Water–Air Interface. The Au NTs@PVP were centrifuged and redispersed in ethanol–hexane at a 2:3 volume ratio. Ethanol was added first, and gentle stirring for a few seconds was required for a successful dispersion. Small amounts of water might affect the stability of the dispersion, leading to phase separation. The self-assembly of the Au NTs was performed as follows: the Au NTs@PVP dispersion was gently placed on top of the pure water surface. Upon evaporation of the organic solvents, the Au NT monolayer became gold-like. Transfer of the Au NT monolayer onto a solid substrate was performed by gently touching it with the substrate parallel to the surface, which is known as "horizontal lifting", or the "Langmuir–Schaeffer" technique. Transfer onto a TEM grid was performed to acquire TEM images. Transfer onto a glass substrate was also performed to get optical photographs, UV–vis

spectra, and SERS measurements. Glass slides (20 × 20 mm^2; Menzel-Gläser, Thermo Scientific, Germany) were thoroughly cleaned by ultrasonication in water with soap, ethanol, and acetone, 15 min for each solvent. After this cleaning procedure, the glass slides were thoroughly rinsed with Milli-Q ultrapure water and gently blow-dried with a stream of N_2 gas. Substrates were stored in sealed Petri dishes.

Sample Preparation for SERS Measurements. The SERS-enhancing performance of the Au NT assemblies was tested using benzenethiol, 4-mercaptopyridine, crystal violet, and 2,4-dinitrotoluene as standard analytes in different concentrations. Consecutive Milli-Q water dilutions of 1 mM BT, 4-MP, and CV ethanol stock solutions were performed to reach final concentrations of 100, 10, 1, and 0.1 μM. The BT stock solution was freshly prepared prior to each SERS measurement. For SERS measurements in solution, the Au NT colloids were stabilized in 0.1 mM CTAC to prevent aggregation, and the nanoparticle concentration set to [Au^0] = 0.5 mM. A 4 μL amount of BT and CV stock (100, 10, and 1 μM) was added to 400 μL of Au NT solutions, respectively. For SERS measurements of CV on solid samples, after deposition of the Au NTs@PVP, the glass slides were treated with UV/ozone (UV/Ozone ProCleaner; Bioforce Nanoscience, Ames, IA, USA) for 30 min, and 7 μL of analyte solution evenly spread over the assembled Au NTs and the SERS spectra was collected after complete drying overnight. For SERS measurements of BT on solid samples, prior to PVP coating and monolayer formation, the analyte was preincubated in solution overnight with the Au NTs@CTAC. All spectra were background corrected except for CV. The background spectra were recorded by measuring the SERS signal of the nanoparticle assembly without analyte, to discriminate possible contributions originating from residues of the polymer or its fragments.

Spectroscopic, SERS, and Structural Characterization. Transmission electron microscopy (TEM) images were collected with a JEOL JEM-1400PLUS instrument operating at 120 kV, using carbon-coated 400 square mesh copper grids; all samples were centrifuged twice before dropping it on the TEM grid. SEM images were collected with a Zeiss Ultra 55 FEG SEM, operated at 10 kV. SEM samples were prepared by spin-coating the collodial solutions on silicon substrates, previously cleaned with piranha solution. Optical extinction spectra were recorded using an Agilent 8453 UV−vis diode-array spectrophotometer. All the presented UV−vis spectra were multiplied by the respective dilution factors to facilitate comparison of the data. SERS spectra were recorded using a Renishaw Invia Raman microscope equipped with two Peltier-cooled CCD detectors, a Leica microscope with two gratings with 1200 and 1800 lines/mm and band-pass filter optics. For SERS measurements, a diode laser with emission wavelengths of 633 and 785 nm was used and focused onto the liquid sample through an objective with a 15 mm focal length and onto the solid sample through a 100× or 50× objective with a NA of 0.34, 0.9, or 0.5, respectively. The liquid samples were irradiated with laser powers of 5 mW (785 nm excitation) and 0.32 mW (633 nm excitation). The solid samples were irradiated with laser powers of 0.2 mW for 785 nm and 10 μW for 633 nm excitation wavelength. In solution, the SERS spectra were collected with an exposition time of 1 s, and 500 (BT and CV) or 300 (4-MP and 2,4-DNT) scans were accumulated. For solid samples, the exposition time was set to 1 s and one scan accumulated. The BT SERS maps were generated by plotting the fitted peak areas of the vibrational modes at 1075 and 1575 cm^{-1}.

Conflict of Interest: The authors declare no competing financial interest.

Supporting Information Available: Additional TEM images, SERS spectra, and schematic graphic descriptions of the synthetic procedures. This material is available free of charge *via* the Internet at http://pubs.acs.org.

Acknowledgment. This work was supported by the European Research Council (ERC Advanced Grant 267867 Plasmaquo). M. C.-P. acknowledges an FPU scholarship from the Spanish Ministry of Education, Culture and Sports. We would like to thank Dr. Yuri A. Diaz-Fernandez from Kasper Moth-Poulsen's group (Chalmer University, Gotheburg) for the HR-SEM images.

REFERENCES AND NOTES

1. Rodríguez-Lorenzo, L.; Álvarez-Puebla, R. A.; Pastoriza-Santos, I.; Mazzucco, S.; Stéphan, O.; Kociak, M.; Liz-Marzán, L. M.; García de Abajo, F. J. Zeptomol Detection Through Controlled Ultrasensitive Surface-Enhanced Raman Scattering. *J. Am. Chem. Soc.* **2009**, *131*, 4616–4618.
2. Liu, Q.; Cui, Y.; Gardner, D.; Li, X.; He, S.; Smalyukh, I. I. Self-Alignment of Plasmonic Gold Nanorods in Reconfigurable Anisotropic Fluids for Tunable Bulk Metamaterial Applications. *Nano Lett.* **2010**, *10*, 1347–1353.
3. Duncan, B.; Kim, C.; Rotello, V. M. Gold Nanoparticle Platforms as Drug and Biomacromolecule Delivery Systems. *J. Controlled Release* **2010**, *148*, 122–127.
4. Wilczewska, A. Z.; Niemirowicz, K.; Markiewicz, K. H.; Car, H. Nanoparticles as Drug Delivery Systems. *Pharmacol. Rep.* **2012**, *64*, 1020–1037.
5. Pallavicini, P.; Chirico, G.; Collini, M.; Dacarro, G.; Donà, A.; D'Alfonso, L.; Falqui, A.; Diaz-Fernandez, Y.; Freddi, S.; Garofalo, B.; *et al*. Synthesis of Branched Au Nanoparticles with Tunable near-Infrared LSPR Using a Zwitterionic Surfactant. *Chem. Commun.* **2011**, *47*, 1315.
6. Pérez-Juste, J.; Pastoriza-Santos, I.; Liz-Marzán, L. M.; Mulvaney, P. Gold Nanorods: Synthesis, Characterization and Applications. *Coord. Chem. Rev.* **2005**, *249*, 1870–1901.
7. DuChene, J. S.; Niu, W.; Abendroth, J. M.; Sun, Q.; Zhao, W.; Huo, F.; Wei, W. D. Halide Anions as Shape-Directing Agents for Obtaining High-Quality Anisotropic Gold Nanostructures. *Chem. Mater.* **2013**, *25*, 1392–1399.
8. Carbó-Argibay, E.; Rodríguez-González, B.; Pacifico, J.; Pastoriza-Santos, I.; Pérez-Juste, J.; Liz-Marzán, L. M. Chemical Sharpening of Gold Nanorods: The Rod-to-Octahedron Transition. *Angew. Chem., Int. Ed.* **2007**, *46*, 8983–8987.
9. Bastús, N. G.; Comenge, J.; Puntes, V. Kinetically Controlled Seeded Growth Synthesis of Citrate-Stabilized Gold Nanoparticles of up to 200 nm: Size Focusing *versus* Ostwald Ripening. *Langmuir* **2011**, *27*, 11098–11105.
10. Grzelczak, M.; Mezzasalma, S. A.; Ni, W.; Herasimenka, Y.; Feruglio, L.; Montini, T.; Pérez-Juste, J.; Fornasiero, P.; Prato, M.; Liz-Marzán, L. M. Antibonding Plasmon Modes in Colloidal Gold Nanorod Clusters. *Langmuir* **2012**, *28*, 8826–8833.
11. Vial, S.; Pastoriza-Santos, I.; Pérez-Juste, J.; Liz-Marzán, L. M. Plasmon Coupling in Layer-by-Layer Assembled Gold Nanorod Films. *Langmuir* **2007**, *23*, 4606–4611.
12. Sau, T. K.; Murphy, C. J. Room Temperature, High-Yield Synthesis of Multiple Shapes of Gold Nanoparticles in Aqueous Solution. *J. Am. Chem. Soc.* **2004**, *126*, 8648–8649.
13. Jana, N. R.; Gearheart, L.; Murphy, C. J. Seed-Mediated Growth Approach for Shape-Controlled Synthesis of Spheroidal and Rod-like Gold Nanoparticles Using a Surfactant Template. *Adv. Mater.* **2001**, *13*, 1389–1393.
14. Nikoobakht, B.; El-Sayed, M. A. Preparation and Growth Mechanism of Gold Nanorods (NRs) Using Seed-Mediated Growth Method. *Chem. Mater.* **2003**, *15*, 1957–1962.
15. Brown, K. R.; Walter, D. G.; Natan, M. J. Seeding of Colloidal Au Nanoparticle Solutions. 2. Improved Control of Particle Size and Shape. *Chem. Mater.* **2000**, *12*, 306–313.
16. Park, K.; Drummy, L. F.; Wadams, R. C.; Koerner, H.; Nepal, D.; Fabris, L.; Vaia, R. A. Growth Mechanism of Gold Nanorods. *Chem. Mater.* **2013**, *25*, 555–563.
17. Edgar, J. A.; McDonagh, A. M.; Cortie, M. B. Formation of Gold Nanorods by a Stochastic "Popcorn" Mechanism. *ACS Nano* **2012**, *6*, 1116–1125.
18. Ye, X.; Zheng, C.; Chen, J.; Gao, Y.; Murray, C. B. Using Binary Surfactant Mixtures To Simultaneously Improve the Dimensional Tunability and Monodispersity in the Seeded Growth of Gold Nanorods. *Nano Lett.* **2013**, *13*, 765–771.
19. Langille, M. R.; Personick, M. L.; Zhang, J.; Mirkin, C. A. Defining Rules for the Shape Evolution of Gold Nanoparticles. *J. Am. Chem. Soc.* **2012**, *134*, 14542–14554.
20. Lohse, S. E.; Burrows, N. D.; Scarabelli, L.; Liz-Marzán, L. M.; Murphy, C. J. Anisotropic Noble Metal Nanocrystal Growth: The Role of Halides. *Chem. Mater.* **2013**, 131002130545000.

21. Millstone, J. E.; Métraux, G. S.; Mirkin, C. A. Controlling the Edge Length of Gold Nanoprisms via a Seed-Mediated Approach. *Adv. Funct. Mater.* **2006**, *16*, 1209–1214.
22. Banholzer, M. J.; Harris, N.; Millstone, J. E.; Schatz, G. C.; Mirkin, C. A. Abnormally Large Plasmonic Shifts in Silica-Protected Gold Triangular Nanoprisms. *J. Phys. Chem. C* **2010**, *114*, 7521–7526.
23. Jana, N. R. Nanorod Shape Separation Using Surfactant Assisted Self-Assembly. *Chem. Commun.* **2003**, 1950–1951.
24. Park, K.; Koerner, H.; Vaia, R. A. Depletion-Induced Shape and Size Selection of Gold Nanoparticles. *Nano Lett.* **2010**, *10*, 1433–1439.
25. Alvarez-Puebla, R. A.; Liz-Marzán, L. M. Traps and Cages for Universal SERS Detection. *Chem. Soc. Rev.* **2012**, *41*, 43.
26. Jain, P. K.; Huang, W.; El-Sayed, M. A. On the Universal Scaling Behavior of the Distance Decay of Plasmon Coupling in Metal Nanoparticle Pairs: A Plasmon Ruler Equation. *Nano Lett.* **2007**, *7*, 2080–2088.
27. Sánchez-Iglesias, A.; Grzelczak, M.; Pérez-Juste, J.; Liz-Marzán, L. M. Binary Self-Assembly of Gold Nanowires with Nanospheres and Nanorods. *Angew. Chem., Int. Ed.* **2010**, *49*, 9985–9989.
28. Dong, A.; Chen, J.; Vora, P. M.; Kikkawa, J. M.; Murray, C. B. Binary Nanocrystal Superlattice Membranes Self-Assembled at the Liquid−air Interface. *Nature* **2010**, *466*, 474–477.
29. Li, Z.; Zhao, W.; Quinn, J.; Rafailovich, M. H.; Sokolov, J.; Lennox, R. B.; Eisenberg, A.; Wu, X. Z.; Kim, M. W.; Sinha, S. K.; *et al*. X-Ray Reflectivity of Diblock Copolymer Monolayers at the Air/Water Interface. *Langmuir* **1995**, *11*, 4785–4792.
30. Zhu, J.; Eisenberg, A.; Lennox, R. B. Interfacial Behavior of Block Polyelectrolytes. 1. Evidence for Novel Surface Micelle Formation. *J. Am. Chem. Soc.* **1991**, *113*, 5583–5588.
31. Mahmoud, M. A.; Tabor, C. E.; El-Sayed, M. A. Surface-Enhanced Raman Scattering Enhancement by Aggregated Silver Nanocube Monolayers Assembled by the Langmuir−Blodgett Technique at Different Surface Pressures. *J. Phys. Chem. C* **2009**, *113*, 5493–5501.
32. Lee, Y. H.; Lee, C. K.; Tan, B.; Rui Tan, J. M.; Phang, I. Y.; Ling, X. Y. Using the Langmuir−Schaefer Technique to Fabricate Large-Area Dense SERS-Active Au Nanoprism Monolayer Films. *Nanoscale* **2013**, *5*, 6404.
33. Jana, N. R.; Gearheart, L.; Murphy, C. J. Wet Chemical Synthesis of High Aspect Ratio Cylindrical Gold Nanorods. *J. Phys. Chem. B* **2001**, *105*, 4065–4067.
34. Gole, A.; Murphy, C. J. Seed-Mediated Synthesis of Gold Nanorods: Role of the Size and Nature of the Seed. *Chem. Mater.* **2004**, *16*, 3633–3640.
35. Liu, M.; Guyot-Sionnest, P. Mechanism of Silver(I)-Assisted Growth of Gold Nanorods and Bipyramids. *J. Phys. Chem. B* **2005**, *109*, 22192–22200.
36. Mason, T. Osmotically Driven Shape-Dependent Colloidal Separations. *Phys. Rev. E* **2002**, *66*.
37. Vrij, A. Demixed Phases of Colloid plus Polymer Systems in a Common Solvent Calculation of the Interfacial Tension. *Phys. A (Amsterdam, Neth.)* **1997**, *235*, 120–128.
38. Evans, D. F.; Wennerström, H. *Colloidal Domain: Where Physics, Chemistry, Biology, and Technology Meet*, 2nd Ed., 1999, ISBN: 978-0-471-24247-5.
39. Aswal, V.; Goyal, P. Counterions in the Growth of Ionic Micelles in Aqueous Electrolyte Solutions: A Small-Angle Neutron Scattering Study. *Phys. Rev. E* **2000**, *61*, 2947–2953.
40. Malliaris, A.; Binana-Limbele, W.; Zana, R. Fluorescence Probing Studies of Surfactant Aggregation in Aqueous Solutions of Mixed Ionic Micelles. *J. Colloid Interface Sci.* **1986**, *110*, 114–120.
41. Huang, M. H.; Chiu, C.-Y. Achieving Polyhedral Nanocrystal Growth with Systematic Shape Control. *J. Mater. Chem. A* **2013**, *1*, 8081–8092.
42. Payne, E. K.; Shuford, K. L.; Park, S.; Schatz, G. C.; Mirkin, C. A. Multipole Plasmon Resonances in Gold Nanorods. *J. Phys. Chem. B* **2006**, *110*, 2150–2154.
43. Walker, D. A.; Browne, K. P.; Kowalczyk, B.; Grzybowski, B. A. Self-Assembly of Nanotriangle Superlattices Facilitated by Repulsive Electrostatic Interactions. *Angew. Chem., Int. Ed.* **2010**, *49*, 6760–6763.
44. Deegan, R. D.; Bakajin, O.; Dupont, T. F.; Huber, G.; Nagel, S. R.; Witten, T. A. Capillary Flow as the Cause of Ring Stains from Dried Liquid Drops. *Nature* **1997**, *389*, 827–829.
45. Saikin, S. K.; Olivares-Amaya, R.; Rappoport, D.; Stopa, M.; Aspuru-Guzik, A. On the Chemical Bonding Effects in the Raman Response: Benzenethiol Adsorbed on Silver Clusters. *Phys. Chem. Chem. Phys.* **2009**, *11*, 9401–9411.
46. Whelan, C. M.; Barnes, C. J.; Walker, C. G. H.; Brown, N. M. D. Benzenethiol Adsorption on Au(111) Studied by Synchrotron ARUPS, HREELS and XPS. *Surf. Sci.* **1999**, *425*, 195–211.
47. Carron, K. T.; Hurley, L. G. Axial and Azimuthal Angle Determination with Surface-Enhanced Raman Spectroscopy: Thiophenol on Copper, Silver, and Gold Metal Surfaces. *J. Phys. Chem.* **1991**, *95*, 9979–9984.
48. Li, S.; Wu, D.; Xu, X.; Gu, R. Theoretical and Experimental Studies on the Adsorption Behavior of Thiophenol on Gold Nanoparticles. *J. Raman Spectrosc.* **2007**, *38*, 1436–1443.
49. Sriram, S.; Bhaskaran, M.; Chen, S.; Jayawardhana, S.; Stoddart, P. R.; Liu, J. Z.; Medhekar, N. V.; Kalantar-Zadeh, K.; Mitchell, A. Influence of Electric Field on SERS: Frequency Effects, Intensity Changes, and Susceptible Bonds. *J. Am. Chem. Soc.* **2012**, *134*, 4646–4653.
50. Song, W.; Wang, Y.; Zhao, B. Surface-Enhanced Raman Scattering of 4-Mercaptopyridine on the Surface of TiO_2 Nanofibers Coated with Ag Nanoparticles. *J. Phys. Chem. C* **2007**, *111*, 12786–12791.
51. Do, W. H.; Chul, J. L.; Dong, Y. K.; Jung, M. J. Adsorption of 2-Mercaptopyridine and 4-Mercaptopyridine on a Silver Surfaces Investigated by SERS Spectroscopy. *J. Ind. Eng. Chem.* **2012**, *18*, 2141–2146.
52. Zhang, L.; Bai, Y.; Shang, Z.; Zhang, Y.; Mo, Y. Experimental and Theoretical Studies of Raman Spectroscopy on 4-Mercaptopyridine Aqueous Solution and 4-Mercaptopyridine/Ag Complex System. *J. Raman Spectrosc.* **2007**, *38*, 1106–1111.
53. Sylvia, J. M.; Janni, J. A.; Klein, J. D.; Spencer, K. M. Surface-Enhanced Raman Detection of 2,4-Dinitrotoluene Impurity Vapor as a Marker To Locate Landmines. *Anal. Chem.* **2000**, *72*, 5834–5840.
54. Le Ru, E. C.; Blackie, E.; Meyer, M.; Etchegoin, P. G. Surface Enhanced Raman Scattering Enhancement Factors: A Comprehensive Study. *J. Phys. Chem. C* **2007**, *111*, 13794–13803.
55. Scarabelli, L.; Grzelczak, M.; Liz-Marzán, L. M. Tuning Gold Nanorod Synthesis through Prereduction with Salicylic Acid. *Chem. Mater.* **2013**, *25*, 4232–4238.
56. Rodríguez-Fernández, J.; Pérez-Juste, J.; Mulvaney, P.; Liz-Marzán, L. M. Spatially-Directed Oxidation of Gold Nanoparticles by Au(III)−CTAB Complexes. *J. Phys. Chem. B* **2005**, *109*, 14257–14261.